# Early detection of drought-stressed stands in Mediterranean forests using machine learning classification models and a rainfall exclusion experiment

Yehuda Yungstein[1,2], Netanel Fishman[1,2], Gil Lerner[1], Gabriel Mulero[1,2], Yaron Michael[1], Assaf Yaakobi[3], Sophie Obersteiner[3], Laura Rez[3], Tamir Klein[3], David Helman[1,2,*]

1. Department of Soil and Water Sciences, Institute of Environmental Sciences, The Robert H. Smith Faculty of Agriculture, Food and Environment, The Hebrew University of Jerusalem, Rehovot 7610001, Israel.
2. The Advanced School for Environmental Studies, The Hebrew University of Jerusalem, Givat Ram, Jerusalem 9190401, Israel.
3. Department of Plant and Environmental Sciences, Weizmann Institute of Science, Rehovot, 7610001, Israel.

* Corresponding author: david.helman@mail.huji.ac.il

**Abstract**

Climate change-driven droughts increasingly threaten Mediterranean forests. Early detection is crucial for mitigating long-term impacts; yet, conventional methods are limited in spatial and temporal coverage. Remote sensing offers a large-scale solution, but its application at the individual-tree level remains limited, particularly in mixed-species forests.

We combined a controlled rainfall exclusion experiment with drone-based hyperspectral imaging and machine learning to classify drought stress at the individual-tree level in a semi-arid Mediterranean forest (Yishi Forest, Israel). Six 0.05-ha plots with five co-occurring tree species were monitored over two hydrological years. Hyperspectral data (274 bands, 400–1000 nm) were used as is and after synthetically simulating Planet, VENμS, and Sentinel-2 bands in three machine learning classification models.

Results show that rainfall was reduced by nearly half in treated plots. Standard physiological metrics—leaf water potential, carbon assimilation, and transpiration—showed limited treatment sensitivity across most species and seasons, whereas hyperspectral-driven machine learning classification models accurately distinguished between drought-treated and control stands. Logistic Regression (LR) outperformed Support Vector Machines (SVM) and Random Forest (RF), reaching an accuracy of 0.85, a recall of 0.94, and an F1 score of 0.83 in classifying treated stands on a held-out test set. High performance persisted after reducing input to 21 bands. Simulated satellite spectral data showed that SVM performed best using VENμS bands (accuracy = 0.74, F1 = 0.73). When applied to real VENμS imagery from three independent forest sites, the model identified areas of high drought risk one to two years before visible canopy decline.

The presented approach offers a scalable and transferable tool for real-time forest drought monitoring, supporting early warning systems amid growing climate pressures.

*Keywords: Drought-risk; forest decline; Remote Sensing; Support Vector Machine; rain exclusion; VENμS*

## 1. Introduction

Climate variability profoundly impacts forest ecosystems worldwide, with increasing frequency and severity of drought events posing a significant threat to forest health and productivity (Allen et al., 2010). Rising temperatures, associated with increased atmospheric $CO_2$, elevate evaporative demand and accelerate soil drying, potentially outweighing any benefits of improved water-use efficiency (Sanginés de Cárcer et al., 2018; Yuan et al., 2019). Moreover, high temperatures disrupt stomatal regulation, causing rapid depletion of soil water reserves. This pushes trees closer to their physiological limits—a trend expected to intensify with continued global warming (Brodribb et al., 2020; Drake et al., 2018; IPCC, 2023; Urban et al., 2017; Zheng et al., 2022). Mediterranean forests, characterized by dry summers and rainy winters, are particularly vulnerable to these changes and are expected to face more intense and prolonged dry periods (Cramer et al., 2018). The increased frequency and severity of droughts in these regions can decrease forest productivity and biodiversity (Essa et al., 2023; Klein et al., 2019). In addition, some tree species may be at risk of hydraulic collapse in mixed Mediterranean forests during severe droughts, underscoring the critical importance of early detection methods to identify vulnerable stands and initiate timely interventions (Italiano et al., 2024). Detecting and monitoring drought stress in forests is crucial for understanding ecosystem responses to climate change and developing effective management strategies (Hartmann et al., 2018).

Remote sensing involves measuring electromagnetic radiation reflected or emitted from objects at various wavelengths. This technique has become invaluable for monitoring forest health and detecting environmental stresses over extensive spatial scales with high temporal resolution (Helman et al., 2019a). These non-invasive techniques enable the assessment of vegetation properties that indicate plant physiological status and stress responses (Helman et al., 2022, 2019b; Mulero et al., 2023; Zarco-Tejada et al., 2021). Several recent studies have demonstrated the application of remote sensing for drought detection in forests, leveraging various spectral bands and vegetation indices.

Asner et al. (2016) demonstrated the utility of airborne imaging spectroscopy for mapping canopy water content and detecting drought-induced tree mortality in California forests (Asner et al., 2016). Zarco-Tejada et al. (2018) used narrow-band hyperspectral indices to detect early signs of water stress in olive orchards, while Hernández-Clemente et al. (2019) combined visible, near-infrared, and thermal data to assess drought-induced physiological changes in Mediterranean oak forests (Hernández-Clemente et al., 2014; Zarco-Tejada et al., 2018). Anderson et al. (2010) used MODIS data to evaluate the 2005 Amazonian drought, revealing relationships between vegetation indices and tree mortality rates (Anderson et al., 2010). Zhang et al. (2017) compared various remote sensing-based drought indices across the Continental United States, noting the effectiveness of vegetation-based indices like VCI for short-term drought conditions (Zhang et al., 2017). Przeździecki et al. (2023) addressed the challenges of applying drought indices in forests by developing a novel approach to calculate the Temperature Vegetation Dryness Index (TVDI) based on temporal changes in soil moisture rather than spatial heterogeneity (Przeździecki et al., 2023). In a study on Mediterranean hardwood forests, Italiano et al. (2023) combined remote sensing indices with tree-ring analysis and wood anatomy, revealing variability in species-specific drought responses and identifying links between canopy cover, hydraulic conductivity, and growth patterns in drought-affected sites (Italiano et al., 2023).

Recent advancements in machine learning algorithms have greatly enhanced the capacity to extract meaningful information from complex remote sensing datasets (Lary et al., 2016; Li et al., 2023). Several studies have demonstrated the effectiveness of various algorithms in identifying drought-affected areas and assessing forest vulnerability. Olano et al. (2021) used Support Vector Machines (SVM) to detect frost defoliation events in European beech forests, while Mohammed et al. (2022) compared multiple algorithms for drought prediction in the eastern Mediterranean (Mohammed et al., 2022; Olano et al., 2021). Cui et al. (2022) employed Long Short-Term Memory models to project evapotranspiration and assess water stress vulnerability in Mediterranean-climate forests. Buthelezi et al. (2022) evaluated several machine-learning techniques for classifying drought-damaged trees using Landsat-derived vegetation indices in subtropical regions. Additionally, machine learning approaches such as random forests (RF), SVM, and artificial neural networks (ANN) have been successfully used to estimate various water-related plant parameters, including leaf water content, leaf water potential, and equivalent water thickness, from both hyperspectral and multispectral remote sensing data (Fishman et al., 2025; Li et al., 2023; Sadiq et al., 2023; Virnodkar et al., 2020).

Despite the increasing use of remote sensing techniques for forest monitoring, which relies mainly on retrospective analyses of natural drought events, a critical gap remains in accurately classifying drought-stressed stands in forests. No study has yet combined high-resolution hyperspectral drone imagery with machine learning algorithms to classify experimentally induced drought stress at the individual tree level in a forest ecosystem. This approach is particularly important for monitoring stands in Mediterranean forests, where the complex composition of multiple tree species and their varied drought sensitivity complicate monitoring efforts (Cramer et al., 2018; Klein et al., 2019).

Here, we combine hyperspectral drone imagery with machine learning algorithms to classify drought stress in a mixed Mediterranean forest under a unique natural controlled rainfall reduction experiment. We compare three machine learning classification algorithms, accounting for heterogeneous responses of co-occurring species, and integrate high-resolution spectral data with physiological measurements across five tree species to develop drought classification models at the individual tree level. We further train new models based on synthetic data from drone-based hyperspectral images based on Sentinel-2, VENμS, and Planet satellite bands.

## 2. Data

### *2.1. Study site and experimental design*

The research was conducted in Yishi Forest, a semi-arid mixed Mediterranean woodland in Israel's Judean foothills (31° 43´N 34° 57´E; Fig. 1). This forest covers approximately 650 hectares and is located 4 kilometers southwest of Beit Shemesh at an average elevation of 300 meters above sea level (Lapidot et al., 2019; Rog et al., 2024). The climate is characterized by a mean annual precipitation of 460 mm, primarily occurring between November and May, based on data from the past two decades. Temperature records from the Israel Meteorological Service indicate a mean annual temperature of 20.4±6.8 °C, with winter (January-March) and summer (June-August) averages of 16.5±1.9 °C and 24.1±7.9 °C, respectively (Israel Meteorological Service). The predominant soil type in Yishi is terra rossa, comprising A and C horizons. The C horizon soil infiltrates fissures within the weathered limestone bedrock. The A horizon depth averages 21 cm, ranging from 16 to 25 cm (Rog et al., 2021).

The vegetation in Yishi Forest includes both planted and native Mediterranean woody species. The planted gymnosperms are *Pinus halepensis* (Pine) and *Cupressus sempervirens* (Cypress), while the indigenous angiosperms include *Quercus calliprinos* (Oak), *Ceratonia siliqua* (Carob), and *Pistacia lentiscus* (Pistacia). These species have been previously investigated in situ for their water relations and carbon management strategies (Rog et al., 2024, 2021). The forest understory supports a diverse community of annual plants, which flourish during the winter-spring period.

The rainfall exclusion experiment started in November 2021 and was conducted in six 0.05-hectare plots within the forest, each containing the five co-occurring woody species (Fig. 1b,c). Three plots were subjected to rainfall reduction, while three served as controls. The drought simulation employed an open-pipe harvesting system with gutters (Fig. 1d,e) to divert approximately 50% of incident precipitation from treated plots. Soil moisture sensors (EC-5; Meter; Pullman, WA, USA) monitored treatment efficacy, aiming to reduce soil moisture content by 50% compared to control plots. Sensors determined volumetric water content by measuring the dielectric constant of the media using capacitance/frequency domain technology. Five sensors were installed in each stand, in locations under tree canopies and between trees, in undisturbed soil volumes at depths of 15-20 cm below the surface. In each stand, the five sensors were connected to a datalogger (ZL6; Meter; Pullman, WA, USA), which recorded measurements at an hourly resolution and was downloaded during field measurement days.

[Figure 1]

*2.2. Field measurements*

To monitor trees' physiological response to rainfall reduction, three key parameters were assessed: leaf water potential ($\psi_{\mathrm{leaf}}$), assimilation rate ($A_{\mathrm{n}}$), and transpiration rate ($T_{\mathrm{r}}$). These measurements provided insights into the trees' water relations status and photosynthetic activity under varying rainfall conditions (Blackman et al., 2009; Flexas et al., 2004).

$\psi_{\mathrm{leaf}}$ was measured using the pressure chamber method (Boyer, 1967). This technique involves sealing a leaf petiole within a chamber and incrementally raising the internal pressure until sap emerges from the cut end of the petiole. The pressure at this point equals the negative of the $\psi_{\mathrm{leaf}}$, which directly measures the leaf's hydration status (Ritchie and Hinckley, 1975).

$\psi_{\mathrm{leaf}}$ measurements were conducted monthly from October 2021 to March 2023. Sampling was conducted between 11 AM and 1 PM to capture peak daily $\psi_{\mathrm{leaf}}$ values, with the specific time adjusted seasonally. In each plot, one leaf per species was sampled to ensure consistent conditions across species. To minimize measurement errors due to time lags, excised leaves were immediately sealed in airtight plastic bags and kept cool. For analysis, ~30 leaves were sampled per measurement date using a PMS1515 pressure chamber (PMS, Albany, OR, USA). In total, 480 leaf samples were collected over the study period.

In addition to $\psi_{leaf}$, gas exchange parameters were measured to assess the trees' physiological responses to the rainfall reduction treatment. $A_n$ and $T_r$ were measured monthly from October 2021 to March 2023 on clear sky days using a portable infrared gas analyzer system (IRGA; GFS-3000, Walz). Measurements were conducted on mature leaves concurrently with $\psi_{leaf}$ assessments, allowing for non-destructive, in situ evaluation of gas exchange dynamics.

The GFS-3000 was configured with the following settings: standard leaf chamber (Walz 3010-S), an ambient $CO_2$ concentration of 400 ppm, a flow rate of 750 µmol s$^{-1}$, and an impeller speed of 7 steps. The temperature was set to ambient with a 1°C offset. The projected leaf area relative to the chamber size was calculated and adjusted for each tree species to ensure accurate measurements.

$A_n$, representing $CO_2$ uptake by the leaves, was measured in µmol $CO_2$ m$^{-2}$ s$^{-1}$. $T_r$, indicating leaf transpiration, was recorded in mmol $H_2O$ m$^{-2}$ s$^{-1}$. These measurements provided insights into plant gas exchange dynamics under varying environmental conditions and treatments.

Statistical analyses were performed to examine the effects of the drought treatment on tree physiology. For each measured parameter, t-tests were conducted on control and drought-treated plots within each season (summer: June-August, autumn: September-November, winter: December-February, spring: March-May) to quantify treatment effects on tree physiological responses across seasonally varying conditions.

*2.3. Hyperspectral data acquisition and preprocessing*

Hyperspectral imagery was collected using a Nano-Hyperspec camera (Headwall Photonics) mounted on a DJI Matrice 600 Pro (M600) Hexacopter. The M600, equipped with a Global Navigation Satellite System (GNSS) GPS and an Inertial Measurement Unit (IMU), was operated via a remote-control transmitter and a ground control station. The NanoSpec sensor, a push-broom hyperspectral device, captured 274 spectral bands across 640 spatial pixels within the 400-1000 nm range.

Image acquisition coincided with leaf measurements between 11:00 AM and 1:00 PM. The drone flew 60 m above ground level, yielding a spatial resolution of 2 – 3 cm per pixel. Three flights were required to cover the entire study area. Radiometric calibration employed an in-situ 3x3 m grey-white reflectance panel with three distinct reflectance factors (56%, 30%, and 11%). Geometric corrections were based on a ground GNSS receiver (Trimble SPS585 precision RTK) to collect static geolocation data, enabling post-processing kinematic (PPK) flight trajectory calculations.

Raw hyperspectral image cubes underwent radiometric calibration, geometric corrections, and ortho-mosaicking using SpectralView software (version 3.1.4, Headwall Photonics). A two-stage masking process removed non-representative pixels (Fig. 2). First, pixels with a Normalized Difference Vegetation Index (NDVI; Rouse, 1973) value lower than 0.3 were excluded to eliminate soil and understory vegetation (Fig. 1a). Second, shaded canopy portions were masked using a near-infrared reflectance threshold below 0.07 – 0.2 (Fig. 1b). These NDVI and NIR thresholds were determined through iterative visual inspection to optimize removing extraneous elements while retaining vegetation pixels (Fig. 1c). The masking process was done using the Quantum GIS free software (version- 3.32.3).

[Figure 2]

For each tree, the reflectance values of the remaining pixels were averaged to obtain a single mean reflectance spectrum representative of the entire canopy. To mitigate potential artifacts and anomalies in the spectral signatures, a Savitzky-Golay filter (Savitzky and Golay, 1964) was applied, using a window size of 20 bands and second-order polynomials.

The sampling strategy yielded 25 –30 spectral samples per species for each treatment, with one exception. Due to its understory growth habit, *Pistacia* yielded only four spectral samples from drought-treated plots compared to 22 from control plots. In total, the study comprised 246 samples, consisting of 125 from control plots and 121 from the rainfall reduction treatments.

*2.4. Synthetic and actual satellite data*

To enhance the approach's applicability, we used the bands of three high-resolution satellites: Sentinel-2, VENµS, and Planet. We synthetically produced the satellite-equivalent bands from the drone's hyperspectral images, which fall within the same 400–1000 nm range as our Headwall Photonics' hyperspectral camera (Table 1).

[Table 1]

Synthetic bands were created for each satellite by averaging the hyperspectral data over the wavelengths corresponding to each satellite band to train and evaluate the models. We further used the model with actual satellite data (for the optimal satellite/model combination) at three additional Mediterranean forest sites along the rainfall gradient in Israel (see Section 3.3 below), providing insights into the model's ability to detect early drought-stressed stands using real satellite data.

Following the results of the synthetic model evaluation, we obtained actual satellite imagery of the best satellite platform for the three case study sites (Tzora Forest (Tz), Shacharia Forest (Sh), and Gilboa Forest (G) shown in Fig. 1a). Data was downloaded from the Israel VENµS data portal, maintained by Ben-Gurion University of the Negev (https://venus.bgu.ac.il/venus/) for: Tz site, dates 11/9/18, 19/9/19, 19/9/20, site G – 1/12/17, 1/9/2018, 4/9/20, and site Sh – 1/9/18, 2/9/19, 4/9/20. Images were obtained from identical months across multiple years to control for phenological and seasonal variability, spanning three key temporal phases: pre-drought conditions, drought year, and post-drought management intervention periods as documented by JNF (see Section 3.3 and Fig. S1). Level-2 products were downloaded, providing surface reflectance after atmospheric correction for single-day acquisitions at a spatial resolution of 5 m. The data were provided in ready-to-use GeoTIFF format, and no additional preprocessing was required prior to analysis.

## 3. Methods

### *3.1. Machine learning classification models*

We tested three machine learning classification algorithms to build a model that distinguishes drought from control stands using only hyperspectral data: Logistic Regression (LR), Support Vector Machine (SVM), and Random Forest (RF). LR estimates the probability of an outcome using a linear model based on input variables (Cox, 1958), SVM identifies the hyperplane that best separates classes in a high-dimensional space (Cortes and Vapnik, 1995), and RF constructs multiple decision trees and assigns the class that is the mode of the classes predicted by these trees (Breiman, 2001).

Input features comprised average canopy reflectance values across 274 hyperspectral bands, for the hyperspectral data models, and fewer bands, for the satellite synthetic data model (see Table 1). The predicted variable consisted of 246 samples, comprising 125 controls and 121 drought samples, which were randomly partitioned into a training set (70%, N=172) and a held-out test set (30%, N=74), with reproducibility ensured through a fixed random state.

#### 3.1.1. Hyperparameter selection

Model hyperparameters were systematically optimized to enhance performance and mitigate overfitting, using a randomized search strategy coupled with cross-validation restricted to the training dataset.

For LR, optimization employed a *3*-fold cross-validation scheme across 50 iterations, with accuracy as the optimization metric. The hyperparameter space included penalty type, inverse regularization strength, solver algorithm, convergence tolerance, intercept inclusion, and intercept scaling factor (applicable only with specific solver and intercept configurations), as well as maximum iterations ranging from 100 to 500.

For SVM, accuracy optimization used a 3-fold cross-validation across 50 iterations. The hyperparameter space encompassed the following options: kernel type (linear, polynomial, radial basis function, and sigmoid), shrinking heuristic utilization, regularization parameter, kernel coefficients relevant for polynomial and sigmoid kernels, polynomial degree for polynomial kernels, and convergence tolerance.

For RF, hyperparameter optimization employed a *3*-fold cross-validation scheme across 50 iterations, with accuracy as the optimization metric. Optimized parameters included the number of trees ranging from 200 to 2000, a split quality criterion based on either Gini impurity or entropy, maximum tree depth, minimum samples required for node splitting, minimum samples required per leaf node, and the number of features considered for optimal splitting. The search used all available processor cores.

#### 3.1.2. Feature selection

We implemented a multi-step approach to address potential overfitting due to the high dimensionality of the data for models using all 274 spectral bands (for only 246 samples), as described below. Models using the satellite synthetic data did not require dimensionality reduction.

To facilitate this dimensionality reduction, feature importance was quantified for each model trained on the training set (N = 172). The method for calculating importance varied by algorithm:

For the LR model, importance was calculated as the absolute value of the fitted coefficients, normalized to represent the percentage contribution of each spectral band. For the RF model, the intrinsic mean decrease in impurity, also known as Gini importance, was calculated during training and normalized to percentages. For the SVM, which used the optimized kernel and required probability estimates, feature importance was estimated using Permutation Importance. This involved measuring the mean decrease in model accuracy on the training data when the values of individual features were randomly permuted across 10 repeats. The resulting mean importance scores were normalized to percentages.

Feature selection was then performed for each model. Features accounting for 80% of the cumulative importance were retained. If the number of selected features exceeded 25 bands (10% of the sample size), an additional filter was applied to retain only the most significant band within each 10 nm range. Following feature selection, models were retrained using this reduced feature set, with random hyperparameter search and k-fold cross-validation applied again.

Final evaluations of these refined models were conducted on the test set using the metrics above to assess their generalizability to unseen data. The final evaluation of these refined models was conducted on the held-out test set using standard classification metrics: Accuracy, Recall, Precision, and F1 Score, defined in Section 3.2. In addition to these metrics, the distribution of predicted probabilities for the 'drought' class, generated using probability estimation on the test set, was examined for each model. Histograms comparing the distributions for control versus drought actual samples were plotted to assess class separability and analyze misclassification patterns.

Figure 3 summarizes the entire modeling scheme.

[Fig. 3 – Modeling schemes]

### *3.2. Statistical analyses*

$\psi_{\text{leaf}}$, *A*n, and $T_{\text{r}}$ measurements were tested for normality at p > 0.05 sample with the Shapiro–Wilk test using the JMP 17 Pro statistical software (SAS Institute) before applying the t-test. All tests for statistical significance of model performance were performed within the Python pipeline at p < 0.05. All ML models were implemented using the scikit-learn library (Version 1.6.1; Pedregosa et al., 2011) within a Python (Version 3.11.12) environment.

Model performance was assessed using Accuracy, Recall, Precision, and F1 Score metrics. These metrics are calculated as follows:

$$\text{Accuracy} = \frac{\text{TP} + \text{TN}}{\text{TP} + \text{TN} + \text{FP} + \text{FN}} \quad (1)$$

$$\text{Recall} = \frac{\text{TP}}{\text{TP} + \text{FN}} \quad (2)$$

$$\text{Precision} = \frac{TP}{TP + FP} \qquad (3)$$

$$\text{F1 Score} = 2 \times \frac{\text{Precision} \times \text{Recall}}{\text{Precision} \times \text{Recall}} \qquad (4)$$

where TP denotes True Positives, TN denotes True Negatives, FP denotes False Positives, and FN denotes False Negatives. Accuracy measures the proportion of correct predictions (both true positives and true negatives) among the total number of cases examined. Recall, also known as sensitivity, quantifies the proportion of actual positive cases that were correctly identified. In our context, it represents the model's ability to identify trees under drought stress correctly. Precision measures the proportion of positive predicted positive cases, highlighting the model's ability to accurately identify drought-stressed trees. The F1 Score is the harmonic mean of precision and recall, providing a single score that balances both metrics.

### *3.3. Case studies for model evaluation with actual satellite data*

To validate the efficacy of our best-performing model beyond experimental conditions, we conducted an independent assessment across three geographically distinct Mediterranean forests in Israel: Tzora Forest (Tz), Shacharia Forest (Sh), and Gilboa Forest (G) (Fig. 1a). This approach enabled evaluation of the model's transferability to actual satellite imagery for detecting naturally occurring drought stress across diverse environmental gradients. The evaluation sites represent a range of varied microclimatic conditions within Israel's Mediterranean forest ecosystem. The Tz site has a mean annual temperature of 20.5 ± 6.8 °C and a relative humidity of 60.6 ± 21.9 %. The Sh site has a mean annual temperature of 20.7 ± 7.1 °C and a relative humidity of 67.0 ± 21.0%. G site has a mean annual temperature of 19.1 ± 7.0 °C and a relative humidity of 66.5 ± 23.9%.

To quantify drought occurrence at each site, we analyzed annual precipitation data from the nearest Israel Meteorological Service (IMS) stations, at distances of 5.8 km, 4.8 km, and 7.5 km from Tzora, Shacharia, and Gilboa forests, respectively. 2017 saw a severe drought in all three sites (Fig. S1). Thus, we selected this year for our model evaluation and searched for signs of forest decline in subsequent years, looking for overlapping areas marked as stressed according to the model.

Following the comparative analysis of hyperspectral-derived synthetic satellite bands, we used the satellite platform that yielded the highest classification accuracy in our experimental setup to produce drought risk maps for the three sites (Tz, Sh, and G). The optimal classification model, as determined from our experimental site analysis, was applied directly to the raw satellite imagery. The model generated pixel-level drought probability scores ranging from 0 (low drought probability) to 1 (high drought probability) across the site.

## 4. Results

### *4.1. Field observations*

The soil water content was consistently lower at the rain-exclusion plots during the entire period (Fig. 4). The average reduction was 47.2%, implying that nearly half of the rain did not reach the ground in these plots.

[Figure 4]

However, it seems that such a reduction did not affect the $\psi_{leaf}$ in most stands (Fig. 5), except the oak that exhibited more negative values during summer and autumn (Fig. 5c) and the pine that showed lower values during the spring (Fig. 5d). The t-tests verified that the reduction of almost half the incoming water did not affect the apparent tree physiology. At least not via $\psi_{leaf}$, $A_n$ and $T_r$ for most of the season and most species (Table 2).

[Figure 5]

[Table 2]

*4.2. Machine learning classification models*

The classification models, however, showed a significant difference among the spectroscopy of drought and control stands (Table 3). The best model was the linear model (LR), with an accuracy of 0.85, a recall of 0.94, and an F1 score of 0.83. LR was the best-performing algorithm even when the number of bands was reduced to 80% of the most important bands, from 274 bands to only 21 bands.

[Table 3]

The LR was not only the best model, but it also showed to perform extremely accurate in separating drought from control stands, with only few overlapping cases (Fig. 6). Most misclassified cases were within the $\pm 20\%$ overlapping zone (i.e., between 0.3 and 0.7; Fig. S2a), with only three false positive (i.e., undetected drought stands) cases (Fig. S2b).

[Figure 6]

*4.3. Satellite synthetic and actual data*

The best model for the satellite synthetic data was, in this case, the SVM (Table 4). Statistics show that SVM had a better performance with the bands of almost all the three satellites. However, Venµs outperformed other satellites with an accuracy of 0.74 and F1 of 0.73. There was no significant difference in the importance of the bands, with B12 (900 – 920 nm) being the most important (10%), and B2 (400 – 440 nm), the least (7%; Fig. S3).

[Table 4]

Using the SVM model with the actual Venµs satellite imagery data for December 2017, showed specific areas in all three sites with a high degree of drought-stress risk (red areas in Fig. 7). The RGB images of the same date, however, did not indicate forest decline or particular stands at risk. Nevertheless, the Tzora site exhibited severe tree mortality the following year (as observed in the aerial image and reported by the JNF), almost precisely in the same area predicted to be at high risk by the SVM model. The same observation was made two years later at the Shacharia and Gilboa sites. Once the damage was visible (in the RGB images), the model no longer indicated drought-stress risk zones (Fig. 7).

[Figure 7]

## 5. Discussion

Accurate canopy-level detection of incipient drought stress in Mediterranean forests stands is critical for implementing timely intervention strategies in increasingly water-limited environments. This study demonstrates that hyperspectral imaging coupled with advanced machine learning algorithms enables the identification of water stress signatures before conventional physiological metrics indicate drought conditions, representing a promising advancement in precision forest monitoring methodologies.

The rainfall exclusion successfully reduced soil water content by approximately ~47% in the treatment plots, clearly establishing differential water availability conditions. However, this substantial reduction in water availability did not translate into consistent, detectable differences in physiological parameters for most species and seasons (Table 2). These findings align with previous studies, indicating Mediterranean woody species possess diverse adaptive mechanisms to cope with seasonal water shortages (Klein et al., 2019; Lloret et al., 2004). The observed physiological resilience may be attributed to: (i) leaf-level measurements inadequately capturing integrated canopy responses (Zarco-Tejada et al., 2018), (ii) deep root systems accessing water beyond monitored soil layers (Rog et al., 2021), and (iii) efficient water-use strategies maintaining physiological function despite reduced water availability (Brodribb et al., 2020; Liu et al., 2015).

Species-specific sensitivity was evident despite overall resilience. Oak species exhibited lower $\psi_{\mathrm{leaf}}$ during the summer and autumn periods (Fig. 5c), while Pine showed reduced $\psi_{\mathrm{leaf}}$ in spring (Fig. 5d; Table 2). This differential sensitivity is consistent with studies showing that Mediterranean species vary in their hydraulic thresholds and drought response strategies (Italiano et al., 2024; Liu et al., 2015). For instance, while the oak's response here was limited to $\psi_{\mathrm{leaf}}$ changes, long-term experimental drought has been shown to significantly reduce aboveground biomass increment in Quercus ilex (Liu et al., 2015), indicating that sustained water deficit, even if not immediately reflected in all physiological metrics, can have cumulative impacts on growth. Similarly, the observed spring sensitivity in Pine could be an early indicator of this genus's known vulnerability to drought-induced mortality in the region, which often becomes apparent under more severe or prolonged water stress (Klein et al., 2019).

Notably, despite limited detection through conventional physiological measurements, our machine learning models successfully identified distinct spectral signatures associated with rainfall reduction treatment using canopy-level hyperspectral data. This indicates that hyperspectral imaging captures subtle, integrated changes in vegetation optical properties induced by water stress, potentially reflecting biochemical changes, alterations in canopy water content (Asner et al., 2016), or structural adjustments such as changes in LAI (Hernández-Clemente et al., 2014) before pronounced physiological symptoms become apparent at the leaf level (Zarco-Tejada et al., 2018).

The superior performance of the LR model (accuracy = 0.82, recall = 0.91; Table 3) indicates that hyperspectral imagery effectively captures drought-induced vegetation changes, even when conventional physiological measurements detect minimal differences. This linear model outperformed more complex algorithms when applied to high-resolution spectral data. The maintenance of high classification accuracy with only 21 bands reduced from 274 demonstrates the efficiency of targeted spectral monitoring, with important practical implications for operational drought detection systems. The high recall value (0.91) is particularly valuable for early warning systems where missed detections could preclude timely management interventions.

The efficacy of LR with hyperspectral data likely stems from the nature of the classification problem at high spectral resolution. Hyperspectral data retain narrow absorption features that create a nearly linear separation boundary between drought and control classes, allowing a weighted sum of key bands to effectively distinguish between treatments (Peñuelas et al., 1993). Additionally, the L1-regularized LR performs embedded feature selection, making it particularly well-suited for high-dimensional data with hundreds of potentially correlated bands, as evidenced by its robust performance even after dimensionality reduction.

The consistently suboptimal RF performance (accuracy=0.62; Table 3) can be attributed to several factors: tree-split algorithms lack the global regularization necessary for high-dimensional correlated data; with 246 samples distributed across 274 bands, RF requires stronger signals to rise above random splits; and the limited data per terminal node leads to either high-variance predictions or overly pruned trees. These findings contrast with previous studies by Buthelezi et al. (2022) and Mohammed et al. (2022), which reported favorable results using RF for drought classification, though in different forest ecosystems with larger datasets (Buthelezi et al., 2022; Mohammed et al., 2022).

When extending our approach to satellite-compatible spectral resolutions, the Support Vector Machine algorithm demonstrated superior performance across all three simulated satellite platforms (Table 4), with VENμS satellite bands yielding the best results (accuracy = 0.74, F1 = 0.73). This represents a moderate reduction in performance compared to the full hyperspectral dataset, but remains promising for operational applications given the wider coverage and regular revisit times of satellite platforms. While broader vegetation indices derived from satellites, such as the Vegetation Condition Index (VCI), are used for monitoring general drought conditions across large areas, their performance can vary significantly depending on the region and land cover (Zhang et al., 2017). Our approach focuses on identifying physiological stress spectrally at a finer scale before such indices might show significant changes.

The shift in optimal algorithm from LR with hyperspectral to SVM with satellite-simulated data reflects a fundamental transformation in the classification problem. Aggregated satellite bands blur the narrow absorption features that enable linear separation in hyperspectral data, resulting in classification that now relies on non-linear interactions between bands, which SVM, with its polynomial kernel, can effectively capture. The versatility of SVM for analyzing forest stress using satellite data has also been demonstrated in other contexts, such as detecting frost defoliation (Olano et al., 2021). RF models continued to underperform across all satellite platforms (Table 4), with accuracies ranging from 0.51-0.61, substantially below both SVM and LR models. Even with reduced dimensionality, RF struggled with the same fundamental limitations: our relatively modest sample size (n = 246) provided insufficient data for stable tree construction across even the reduced feature space (Barreñada et al., 2024; Han et al., 2021).

The relative uniformity in band importance observed for the VENμS satellite, with B12 (900-920 nm) being only marginally more important at 10% (Figure S3), suggests that the drought signal is distributed across multiple spectral regions rather than concentrated in specific bands.

The model's ability to identify drought-stressed zones 1-2 years before visible forest decline represents the study's most significant contribution. The SVM model applied to VENμS satellite imagery successfully predicted areas of high drought-stress risk in all three test sites, which subsequently experienced severe tree mortality (Fig. 7), despite showing no visual symptoms in RGB imagery at the time of prediction.

This early detection capability advances traditional monitoring, extending pre-visual spectral stress detection (Zarco-Tejada et al., 2018) to operational satellite platforms in Mediterranean forests. Notably, the model identified high-risk zones before visible damage appeared but ceased predictions post-decline, indicating sensitivity to active physiological stress rather than advanced symptoms. This temporal specificity aligns with studies linking spectral data and machine learning to physiological indicators, like earlywood hydraulics (Italiano et al., 2023) or $\psi_{\text{leaf}}$ (Fishman et al., 2025) in Mediterranean forests, and more broadly to water stress assessments (Sadiq et al., 2023; Virnodkar et al., 2020).

The model's ability to predict drought stress in unseen areas, areas excluded from the training set, indicates its generalization and robustness.

### *5.1. Limitations and future directions*

Several limitations warrant consideration. First, our experimental drought simulation, although substantial, may not fully replicate the complex dynamics of natural drought events, which involve interactions between water limitation, heat stress, and extended duration(Allen et al., 2010; IPCC, 2023). Large-scale natural droughts, such as the 2005 Amazonian event analyzed using MODIS data by Anderson et al. (2010), often involve widespread, heterogeneous impacts and mortality patterns that are challenging to fully replicate experimentally (Anderson et al., 2010). Second, our model identified drought stress within a single growing season. Yet, longer-term monitoring would enhance understanding of how spectral signatures evolve over extended drought periods and seasonal cycles.

The performance reduction when moving from hyperspectral to multispectral satellite data indicates that some drought-related spectral information is lost at coarser resolutions. Future research should assess model performance over multiple years, explore its applicability in diverse biomes, leverage higher spectral resolution satellite data as they become available, and integrate complementary sensors, such as thermal imaging or LiDAR, to potentially enhance accuracy (Jimenez-Berni et al., 2018; Przeździecki et al., 2023).

## 6. Conclusions and implications

This study demonstrates that machine learning classification models applied to hyperspectral and multispectral satellite data can effectively detect early signs of drought stress in Mediterranean forests, even when traditional physiological measurements fail to indicate water-related stress. Our findings have several important implications for forest management and conservation strategies.

The early detection capability we demonstrated could significantly improve the timing and targeting of intervention measures, such as selective thinning or emergency irrigation, potentially preventing large-scale forest dieback events. As climate change intensifies drought frequency and severity in Mediterranean regions, such early warning systems become increasingly valuable for preserving forest ecosystem services and biodiversity.

The operational implementation of our approach is facilitated by the developed Streamlit application, available at https://drought-risk-ml-analyzer.streamlit.app/, which allows users to upload VENµS or Sentinel-2 satellite data and receive drought risk assessments without specialized remote sensing expertise. This technology transfer addresses a significant gap between research advancements and practical applications.

**Acknowledgments**

We thank Gil Lerner for flying the drone and assisting with fieldwork, and Itzik Ben-Shabbat from IDO for helping with the drone and flight permits. We also thank the Jewish National Fund (KKL) for supporting this study via KKL Chief Scientist Grant #2145 (430/21). N.F. thanks KKL for the Appleby Award. Y.Y. is a Ph.D. student, N.F. is an M.Sc. student, both from the Faculty of Agriculture, Food, and Environment, Hebrew University, under the supervision of D.H.

## References


Allen, C.D., Macalady, A.K., Chenchouni, H., Bachelet, D., McDowell, N., Vennetier, M., Kitzberger, T., Rigling, A., Breshears, D.D., Hogg, E.H. (Ted), Gonzalez, P., Fensham, R., Zhang, Z., Castro, J., Demidova, N., Lim, J.-H., Allard, G., Running, S.W., Semerci, A., Cobb, N., 2010. A global overview of drought and heat-induced tree mortality reveals emerging climate change risks for forests. For. Ecol. Manage. 259, 660–684. https://doi.org/https://doi.org/10.1016/j.foreco.2009.09.001

Anderson, L.O., Malhi, Y., Aragão, L.E.O.C., Ladle, R., Arai, E., Barbier, N., Phillips, O., 2010. Remote sensing detection of droughts in Amazonian forest canopies. New Phytol. 187, 733–750. https://doi.org/10.1111/j.1469-8137.2010.03355.x

Asner, G.P., Brodrick, P.G., Anderson, C.B., Vaughn, N., Knapp, D.E., Martin, R.E., 2016. Progressive forest canopy water loss during the 2012-2015 California drought. Proc. Natl. Acad. Sci. U. S. A. 113, E249-55. https://doi.org/10.1073/pnas.1523397113

Barreñada, L., Dhiman, P., Timmerman, D., Boulesteix, A.-L., Van Calster, B., 2024. Understanding overfitting in random forest for probability estimation: a visualization and simulation study. Diagnostic Progn. Res. 8, 14. https://doi.org/10.1186/s41512-024-00177-1

Blackman, C.J., Brodribb, T.J., Jordan, G.J., 2009. Leaf hydraulics and drought stress: response, recovery and survivorship in four woody temperate plant species. Plant, cell \& Environ. 32 11, 1584–1595.

Boyer, J.S., 1967. Leaf Water Potentials Measured with a Pressure Chamber. Plant Physiol. 42, 133–137. https://doi.org/10.1104/pp.42.1.133

Breiman, L., 2001. Random Forests. Mach. Learn. 45, 5–32. https://doi.org/10.1023/A:1010933404324

Brodribb, T.J., Powers, J., Cochard, H., Choat, B., 2020. Hanging by a thread? Forests and drought. Science (80-. ). 368, 261–266. https://doi.org/10.1126/science.aat7631

Buthelezi, M.N.M., Lottering, R.T., Hlatshwayo, S.T., Peerbhay, K.Y., 2022. Localizing the analysis of drought impacts on KwaZulu-Natal’s commercial forests. Remote Sens. Appl. Soc. Environ. 28, 100849. https://doi.org/https://doi.org/10.1016/j.rsase.2022.100849

Cortes, C., Vapnik, V., 1995. Support-vector networks. Mach. Learn. 20, 273–297. https://doi.org/10.1007/BF00994018

Cox, D.R., 1958. The Regression Analysis of Binary Sequences. J. R. Stat. Soc. Ser. B 20, 215–232. https://doi.org/10.1111/j.2517-6161.1958.tb00292.x

Cramer, W., Guiot, J., Fader, M., Garrabou, J., Gattuso, J.-P., Iglesias, A., Lange, M.A., Lionello, P., Llasat, M.C., Paz, S., Peñuelas, J., Snoussi, M., Toreti, A., Tsimplis, M.N., Xoplaki, E., 2018. Climate change and interconnected risks to sustainable development in the Mediterranean. Nat. Clim. Chang. 8, 972–980. https://doi.org/10.1038/s41558-018-0299-2

Cui, G., Ma, Q., Bales, R., 2022. Assessing multi-year-drought vulnerability in dense Mediterranean-climate forests using water-balance-based indicators. J. Hydrol. 606, 127431. https://doi.org/https://doi.org/10.1016/j.jhydrol.2022.127431

Drake, J.E., Tjoelker, M.G., Vårhammar, A., Medlyn, B.E., Reich, P.B., Leigh, A., Pfautsch, S., Blackman, C.J., López, R., Aspinwall, M.J., Crous, K.Y., Duursma, R.A., Kumarathunge, D., De Kauwe, M.G., Jiang, M., Nicotra, A.B., Tissue, D.T., Choat, B., Atkin, O.K., Barton, C.V.M., 2018. Trees tolerate an extreme heatwave via sustained transpirational cooling and increased leaf thermal tolerance. Glob. Chang. Biol. 24, 2390–2402. https://doi.org/10.1111/gcb.14037

Essa, Y.H., Hirschi, M., Thiery, W., El-Kenawy, A.M., Yang, C., 2023. Drought characteristics in Mediterranean under future climate change. npj Clim. Atmos. Sci. 6, 133. https://doi.org/10.1038/s41612-023-00458-4

Fishman, N., Yungstein, Y., Yaakobi, A., Obersteiner, S., Rez, L., Mulero, G., Michael, Y., Klein, T., Helman, D., 2025. Leaf Water Potential in a Mixed Mediterranean Forest from Machine Learning and Unmanned Aerial Vehicle (UAV)-Based Hyperspectral Imaging. Remote Sens. https://doi.org/10.3390/rs17010106

Flexas, J., Bota, J., Loreto, F., Cornic, G., Sharkey, T.D., 2004. Diffusive and metabolic limitations to photosynthesis under drought and salinity in C(3) plants. Plant Biol. (Stuttg). 6, 269–279. https://doi.org/10.1055/s-2004-820867

Han, S., Williamson, B.D., Fong, Y., 2021. Improving random forest predictions in small datasets from two-phase sampling designs. BMC Med. Inform. Decis. Mak. 21, 1–9.

Hartmann, H., Moura, C.F., Anderegg, W.R.L., Ruehr, N.K., Salmon, Y., Allen, C.D., Arndt, S.K., Breshears, D.D., Davi, H., Galbraith, D., Ruthrof, K.X., Wunder, J., Adams, H.D., Bloemen, J., Cailleret, M., Cobb, R., Gessler, A., Grams, T.E.E., Jansen, S., Kautz, M., Lloret, F., O'Brien, M., 2018. Research frontiers for improving our understanding of drought-induced tree and forest mortality. New Phytol. 218, 15–28. https://doi.org/10.1111/nph.15048

Helman, D., Bonfil, D.J., Lensky, I.M., 2019a. Crop RS-Met: A biophysical evapotranspiration and root-zone soil water content model for crops based on proximal sensing and meteorological data. Agric. Water Manag. 211, 210–219. https://doi.org/10.1016/j.agwat.2018.09.043

Helman, D., Lensky, I.M., Bonfil, D.J., 2019b. Early prediction of wheat grain yield production from root-zone soil water content at heading using Crop RS-Met. F. Crop. Res. 232, 11–23. https://doi.org/10.1016/j.fcr.2018.12.003

Helman, D., Yungstein, Y., Mulero, G., Yaron, M., 2022. High-Throughput Remote Sensing of Vertical Green Living Walls ( VGWs ) in Workplaces. Remote Sens. 14. https://doi.org/https://doi.org/10.3390/ rs14143485

Hernández-Clemente, R., Navarro-Cerrillo, R.M., Ramírez, F.J.R., Hornero, A., Zarco-Tejada, P.J., 2014. A Novel Methodology to Estimate Single-Tree Biophysical Parameters from 3D Digital Imagery Compared to Aerial Laser Scanner Data. Remote Sens. https://doi.org/10.3390/rs61111627

IPCC, 2023. Climate Change 2023: Synthesis Report. Contribution of Working Groups I, II and III to the Sixth Assessment Report of the Intergovernmental Panel on Climate Change [Core Writing Team, H. Lee and J. Romero (eds.)]. Geneva, Switzerland. https://doi.org/10.59327/IPCC/AR6-9789291691647.001

Israel Meteorological Service, n.d.

Italiano, S.S.P., Camarero, J.J., Borghetti, M., Colangelo, M., Rita, A., Ripullone, F., 2024. Drought legacies in mixed Mediterranean forests: Analysing the effects of structural overshoot, functional traits and site factors. Sci. Total Environ. 927, 172166. https://doi.org/https://doi.org/10.1016/j.scitotenv.2024.172166

Italiano, S.S.P., Julio Camarero, J., Borghetti, M., Colangelo, M., Pizarro, M., Ripullone, F., 2023. Radial growth, wood anatomical traits and remote sensing indexes reflect different impacts of drought on Mediterranean forests. For. Ecol. Manage. 548, 121406. https://doi.org/https://doi.org/10.1016/j.foreco.2023.121406

Jimenez-Berni, J.A., Deery, D.M., Rozas-Larraondo, P., Condon, A. (Tony) G., Rebetzke, G.J., James, R.A., Bovill, W.D., Furbank, R.T., Sirault, X.R.R., 2018. High Throughput Determination of Plant Height, Ground Cover, and Above-Ground Biomass in Wheat with LiDAR. Front. Plant Sci. 9. https://doi.org/10.3389/fpls.2018.00237

Klein, T., Cahanovitc, R., Sprintsin, M., Herr, N., Schiller, G., 2019. A nation-wide analysis of tree mortality under climate change: Forest loss and its causes in Israel 1948–2017. For. Ecol. Manage. 432, 840–849. https://doi.org/https://doi.org/10.1016/j.foreco.2018.10.020

Lapidot, O., Ignat, T., Rud, R., Rog, I., Alchanatis, V., Klein, T., 2019. Use of thermal imaging to detect evaporative cooling in coniferous and broadleaved tree species of the Mediterranean maquis. Agric. For. Meteorol. 271, 285–294. https://doi.org/10.1016/j.agrformet.2019.02.014

Lary, D.J., Alavi, A.H., Gandomi, A.H., Walker, A.L., 2016. Machine learning in geosciences and remote sensing. Geosci. Front. 7, 3–10. https://doi.org/https://doi.org/10.1016/j.gsf.2015.07.003

Li, J., Wijewardane, N.K., Ge, Y., Shi, Y., 2023. Improved chlorophyll and water content estimations at leaf level with a hybrid radiative transfer and machine learning model. Comput. Electron. Agric. 206, 107669. https://doi.org/https://doi.org/10.1016/j.compag.2023.107669

Liu, D., Ogaya, R., Barbeta, A., Yang, X., Peñuelas, J., 2015. Contrasting impacts of continuous moderate drought and episodic severe droughts on the aboveground-biomass increment and litterfall of three coexisting Mediterranean woody species. Glob. Chang. Biol. 21, 4196–4209. https://doi.org/10.1111/gcb.13029

Lloret, F., Siscart, D., Dalmases, C., 2004. Canopy recovery after drought dieback in holm-oak Mediterranean forests of Catalonia (NE Spain). Glob. Chang. Biol. 10, 2092–2099. https://doi.org/10.1111/j.1365-2486.2004.00870.x

Mohammed, S., Elbeltagi, A., Bashir, B., Alsafadi, K., Alsilibe, F., Alsalman, A., Zeraatpisheh, M., Széles, A., Harsányi, E., 2022. A comparative analysis of data mining techniques for agricultural and hydrological drought prediction in the eastern Mediterranean. Comput. Electron. Agric. 197, 106925. https://doi.org/https://doi.org/10.1016/j.compag.2022.106925

Mulero, G., Jiang, D., Bonfil, D.J., Helman, D., 2023. Use of thermal imaging and the photochemical reflectance index (PRI) to detect wheat response to elevated CO(2) and drought. Plant. Cell Environ. 46, 76–92. https://doi.org/10.1111/pce.14472

Olano, J.M., García-Cervigón, A.I., Sangüesa-Barreda, G., Rozas, V., Muñoz-Garachana, D., García-Hidalgo, M., García-Pedrero, Á., 2021. Satellite data and machine learning reveal the incidence of late frost defoliations on Iberian beech forests. Ecol. Appl. 31, e02288. https://doi.org/10.1002/eap.2288

Pedregosa, F., Varoquaux, G., Gramfort, A., Michel, V., Thirion, B., Grisel, O., Blondel, M., Prettenhofer, P., Weiss, R., Dubourg, V., 2011. Scikit-learn: Machine learning in Python. J. Mach. Learn. Res. 12, 2825–2830.

Peñuelas, J., Filella, I., Biel, C., Serrano, L., Savé, R., 1993. The reflectance at the 950–970 nm region as an indicator of plant water status. Int. J. Remote Sens. 14, 1887–1905. https://doi.org/10.1080/01431169308954010

Przeździecki, K., Zawadzki, J.J., Urbaniak, M., Ziemblińska, K., Miatkowski, Z., 2023. Using temporal variability of land surface temperature and normalized vegetation index to estimate soil moisture condition on forest areas by means of remote sensing. Ecol. Indic. 148, 110088. https://doi.org/https://doi.org/10.1016/j.ecolind.2023.110088

Ritchie, G.A., Hinckley, T.M., 1975. The Pressure Chamber as an Instrument for Ecological Research. Adv. Ecol. Res. 9, 165–254. https://doi.org/10.1016/S0065-2504(08)60290-1

Rog, I., Hilman, B., Fox, H., Yalin, D., Qubaja, R., Klein, T., 2024. Increased belowground tree carbon allocation in a mature mixed forest in a dry versus a wet year. Glob. Chang. Biol. 30, e17172. https://doi.org/10.1111/gcb.17172

Rog, I., Tague, C., Jakoby, G., Megidish, S., Yaakobi, A., Wagner, Y., Klein, T., 2021. Interspecific Soil Water Partitioning as a Driver of Increased Productivity in a Diverse Mixed Mediterranean Forest. J. Geophys. Res. Biogeosciences 126.

Rouse, J.W., 1973. Monitoring the vernal advancement and retrogradation of natural vegetation. NASA/GSFCT Type II Rep.

Sadiq, M.A., Sarkar, S.K., Raisa, S.S., 2023. Meteorological drought assessment in northern Bangladesh: A machine learning-based approach considering remote sensing indices. Ecol. Indic. 157, 111233. https://doi.org/https://doi.org/10.1016/j.ecolind.2023.111233

Sanginés de Cárcer, P., Vitasse, Y., Peñuelas, J., Jassey, V.E.J., Buttler, A., Signarbieux, C., 2018. Vapor-pressure deficit and extreme climatic variables limit tree growth. Glob. Chang. Biol. 24, 1108–1122. https://doi.org/10.1111/gcb.13973

Savitzky, A., Golay, M.J.E., 1964. Smoothing and Differentiation of Data by Simplified Least Squares Procedures. Anal. Chem. 36, 1627–1639. https://doi.org/10.1021/ac60214a047

Urban, J., Ingwers, M.W., McGuire, M.A., Teskey, R.O., 2017. Increase in leaf temperature opens stomata and decouples net photosynthesis from stomatal conductance in Pinus taeda and Populus deltoides x nigra. J. Exp. Bot. 68, 1757–1767. https://doi.org/10.1093/jxb/erx052

Virnodkar, S.S., Pachghare, V.K., Patil, V.C., Jha, S.K., 2020. Remote sensing and machine learning for crop water stress determination in various crops: a critical review. Precis. Agric. 21, 1121–1155. https://doi.org/10.1007/s11119-020-09711-9

Yuan, W., Zheng, Y., Piao, S., Ciais, P., Lombardozzi, D., Wang, Y., Ryu, Y., Chen, G., Dong, W., Hu, Z., Jain, A.K., Jiang, C., Kato, E., Li, S., Lienert, S., Liu, S., Nabel, J.E.M.S., Qin, Z., Quine, T., Sitch, S., Smith, W.K., Wang, F., Wu, C., Xiao, Z., Yang, S., 2019. Increased atmospheric vapor pressure deficit reduces global vegetation growth. Sci. Adv. 5, eaax1396. https://doi.org/10.1126/sciadv.aax1396

Zarco-Tejada, P.J., Camino, C., Beck, P.S.A., Calderon, R., Hornero, A., Hernández-Clemente, R., Kattenborn, T., Montes-Borrego, M., Susca, L., Morelli, M., Gonzalez-Dugo, V., North, P.R.J., Landa, B.B., Boscia, D., Saponari, M., Navas-Cortes, J.A., 2018. Previsual symptoms of Xylella fastidiosa infection revealed in spectral plant-trait alterations. Nat. Plants 4, 432–439. https://doi.org/10.1038/s41477-018-0189-7

Zarco-Tejada, P.J., Poblete, T., Camino, C., Gonzalez-Dugo, V., Calderon, R., Hornero, A., Hernandez-Clemente, R., Román-Écija, M., Velasco-Amo, M.P., Landa, B.B., Beck, P.S.A., Saponari, M., Boscia, D., Navas-Cortes, J.A., 2021. Divergent abiotic spectral pathways unravel pathogen stress signals across species. Nat. Commun. 12, 6088. https://doi.org/10.1038/s41467-021-26335-3

Zhang, L., Jiao, W., Zhang, H., Huang, C., Tong, Q., 2017. Studying drought phenomena in the Continental United States in 2011 and 2012 using various drought indices. Remote Sens. Environ. 190, 96–106. https://doi.org/https://doi.org/10.1016/j.rse.2016.12.010

Zheng, Y., Wu, S., Xiao, S., Yu, K., Fang, X., Xia, L., Wang, J., Liu, S., Freeman, C., Zou, J., 2022. Global methane and nitrous oxide emissions from inland waters and estuaries. Glob. Chang. Biol. 28, 4713–4725. https://doi.org/10.1111/gcb.16233

Table 1. Specifications of sensors used in this study: UAV, Sentinel-2, VENμS, and Planet. The temporal and spatial resolutions, along with the specific spectral bands and their corresponding wavelength ranges, are presented. Only the relevant bands to this research are included.

| Sensor | Temporal Resolution | Spatial Resolution | Bands | Wavelength Range (nm) |
|---|---|---|---|---|
| Matrice 600 Pro Hexacopter (UAV) | ~1 Month | 2–3cm | 274 bands (~2 nm bandwidth) | 400-1000 |
| Sentinel-2 (satellite) | 5 Days | 10m | B2 (Coastal Aerosol) | 443-490 |
| | | | B2 (Blue) | 490-560 |
| | | | B3 (Green) | 560-665 |
| | | | B4 (Red) | 665-705 |
| | | 20m | B5 (Vegetation Red Edge) | 705-740 |
| | | | B6 (Vegetation Red Edge) | 740-783 |
| | | | B7 (Vegetation Red Edge) | 783-842 |
| | | 10m | B8 (NIR) | 842-865 |
| | | 20m | B8A (Narrow NIR) | 865-945 |
| | | | B9 (Water vapor) | 945-1375 |
| VENμS (satellite) | 2 Days | 5m | B2 | 400-440 |
| | | | B3 | 423-463 |
| | | | B4 | 470-510 |
| | | | B5 | 535-575 |
| | | | B6 | 600-640 |
| | | | B7 | 652-682 |
| | | | B8 | 690-714 |
| | | | B9 | 734-750 |
| | | | B10 | 774-790 |
| | | | B11 | 845-885 |
| | | | B12 | 900-920 |
| PlanetScope (satellite) | 1 Day | 3m | Coastal Blue | 433-453 |
| | | | Blue | 465-515 |
| | | | Green I | 513-549 |
| | | | Green | 547-583 |
| | | | Yellow | 600-620 |
| | | | Red | 649-680 |
| | | | Red-Edge | 697-712 |
| | | | NIR | 845-885 |

Table 2. Results of two-sided t-tests comparing the effects of drought and control treatments on leaf water potential ($\psi_{leaf}$), transpiration ($T_r$), and carbon assimilation ($A_n$) for the five woody species across four seasons. P-values from the t-tests are reported, with significant (p<0.05) and marginally significant (0.1 > p > 0.05) effects indicated in bold and italics, respectively.

| Species | Season | $\psi_{leaf}$ (MPa) | $T_r$ (mmol $m^{-2}$ $s^{-1}$) | $A_n$ (μmol $m^{-2}$ $s^{-1}$) |
|---|---|---|---|---|
| *cypress* | Spring | 0.771 | 0.994 | 0.275 |
| | Summer | *0.070* | 0.910 | 0. 542 |
| | Autumn | 0.127 | 0.366 | 0.335 |
| | Winter | 0.770 | 0. 603 | 0.160 |
| *oak* | Spring | 0.751 | 0.127 | 0.428 |
| | Summer | **0.002** | **0.026** | 0.101 |
| | Autumn | *0.066* | 0.133 | 0.472 |
| | Winter | 0.666 | 0.117 | 0.309 |
| *pine* | Spring | **0.010** | 0.249 | 0.927 |
| | Summer | 0.247 | 0.702 | 0.274 |
| | Autumn | 0.589 | 0.797 | 0. 577 |
| | Winter | 0.672 | 0.904 | 0.164 |
| *carob* | Spring | 0.314 | 0.336 | **0.021** |
| | Summer | 0.963 | *0.089* | 0.117 |
| | Autumn | 0.212 | 0.472 | 0.338 |
| | Winter | 0.841 | **0.040** | 0. 643 |
| *pistacia* | Spring | 0.239 | 0.348 | 0.754 |
| | Summer | 0.978 | 0. 628 | 0. 635 |
| | Autumn | 0.381 | 0.989 | 0.294 |
| | Winter | 0.459 | 0.454 | 0.376 |

Table 3. Performance metrics of the three machine learning models for binary classification using hyperspectral drone imagery models trained using either the full spectral range (274 bands, 400-1000 nm) or a reduced set of the most important features (determined by feature importance ranking, retaining 80% of cumulative importance). Each sample represents the spectral signature of an individual tree canopy. The highest score for each performance metric is highlighted in bold.

| Performance Metric | Full Spectral Range (274 Bands) | | | Reduced Features (80% Importance) | | |
|---|---|---|---|---|---|---|
| | **LR** | **SVM** | **RF** | **LR** (21 Bands) | **SVM** (13 Bands) | **RF** (23 Bands) |
| *Accuracy* | **0.85** | 0.81 | 0.59 | **0.82** | 0.68 | 0.62 |
| *Recall* | **0.94** | 0.85 | 0.50 | **0.91** | 0.82 | 0.53 |
| *Precision* | **0.78** | 0.76 | 0.57 | **0.76** | 0.61 | 0.60 |
| *F1 Score* | **0.85** | 0.81 | 0.53 | **0.83** | 0.71 | 0.56 |

Table 4. Performance metrics of the three machine learning models for binary classification using Satellite synthetic bands for PlanetScope, VENµS, and Sentinel-2. The highest score for each satellite and metric is highlighted in bold.

| Satellite | PlanetScope | | | VENµS | | | Sentinel-2 | | |
|---|---|---|---|---|---|---|---|---|---|
| | **LR** | **SVM** | **RF** | **LR** | **SVM** | **RF** | **LR** | **SVM** | **RF** |
| *Accuracy* | 0.55 | **0.65** | 0.61 | 0.64 | **0.74** | 0.54 | 0.54 | **0.70** | 0.51 |
| *Precision* | 0.51 | **0.63** | 0.58 | 0.58 | **0.70** | 0.50 | 0.50 | **0.66** | 0.47 |
| *Recall* | **0.68** | 0.67 | 0.56 | 0.74 | **0.76** | 0.41 | 0.62 | **0.74** | 0.44 |
| *F1 Score* | 0.58 | **0.65** | 0.57 | 0.65 | **0.73** | 0.45 | 0.55 | **0.69** | 0.45 |

Supplementary Table S1. Optimized hyperparameters for Logistic Regression (LR), Support Vector Machine (SVM), and Random Forest (RF). Models were trained on two datasets: complete hyperspectral data (274 bands) and reduced feature sets comprising the top 80% most important bands. The models classified the samples as control or drought-stressed.

| Model | *Hyperparameter* | 274 Bands | 80% Importance Bands |
|---|---|---|---|
| *LR* | C | 458 | 723 |
| | fit_intercept | False | False |
| | intercept_scaling | 0.48 | 0.55 |
| | max_iter | 300 | 500 |
| | penalty | l1 | l1 |
| | solver | liblinear | liblinear |
| | tol | 8.23e-05 | 3093e-04 |
| *SVM* | C | 702 | 1.626 |
| | coef0 | 3.37 | 0.23 |
| | degree | 2 | 7 |
| | gamma | 0.48 | 4.61 |
| | kernel | poly | poly |
| | shrinking | False | False |
| | tol | 2.62e-05 | 7.3e-05 |
| *RF* | n_estimators | 1400 | 200 |
| | min_samples_split | 5 | 2 |
| | min_samples_leaf | 4 | 1 |
| | max_features | sqrt | sqrt |
| | max_depth | 30 | 20 |
| | criterion | entropy | gini |

Supplementary Table S2. Optimized hyperparameters for Logistic Regression (LR), Support Vector Machine (SVM), and Random Forest (RF) models implemented using the scikit-learn library in Python. The models were trained on synthetic satellite data derived from the original 274 hyperspectral bands, simulating the spectral bands of three satellite platforms: PlanetScope, VENμS, and Sentinel-2. The models classified the samples as control or drought-stressed.

| Model | *Hyperparameter* | PlanetScope | VENμS | Sentinel-2 |
|---|---|---|---|---|
| *LR* | C | 81.7 | 3.22 | 1.70 |
| | fit_intercept | False | True | False |
| | intercept_scaling | 0.823 | 0.623 | 1.186 |
| | max_iter | 300 | 200 | 400 |
| | penalty | l1 | none | l2 |
| | solver | liblinear | lbfgs | lbfgs |
| | tol | 1.43e-04 | 3.09e-05 | 1.65e-05 |
| *SVM* | C | 702 | 46.3 | 46.3 |
| | coef0 | 3.37 | 0.75 | 0.75 |
| | degree | 2 | 2 | 2 |
| | gamma | 0.486 | 5.58 | 5.86 |
| | kernel | poly | poly | poly |
| | shrinking | False | True | True |
| | tol | 2.62e-05 | 8.17e-05 | 8.17e-05 |
| *RF* | n_estimators | 1800 | 200 | 200 |
| | min_samples_split | 2 | 2 | 2 |
| | min_samples_leaf | 1 | 1 | 1 |
| | max_features | sqrt | auto | sqrt |
| | max_depth | 50 | 50 | 110 |
| | criterion | gini | gini | entropy |

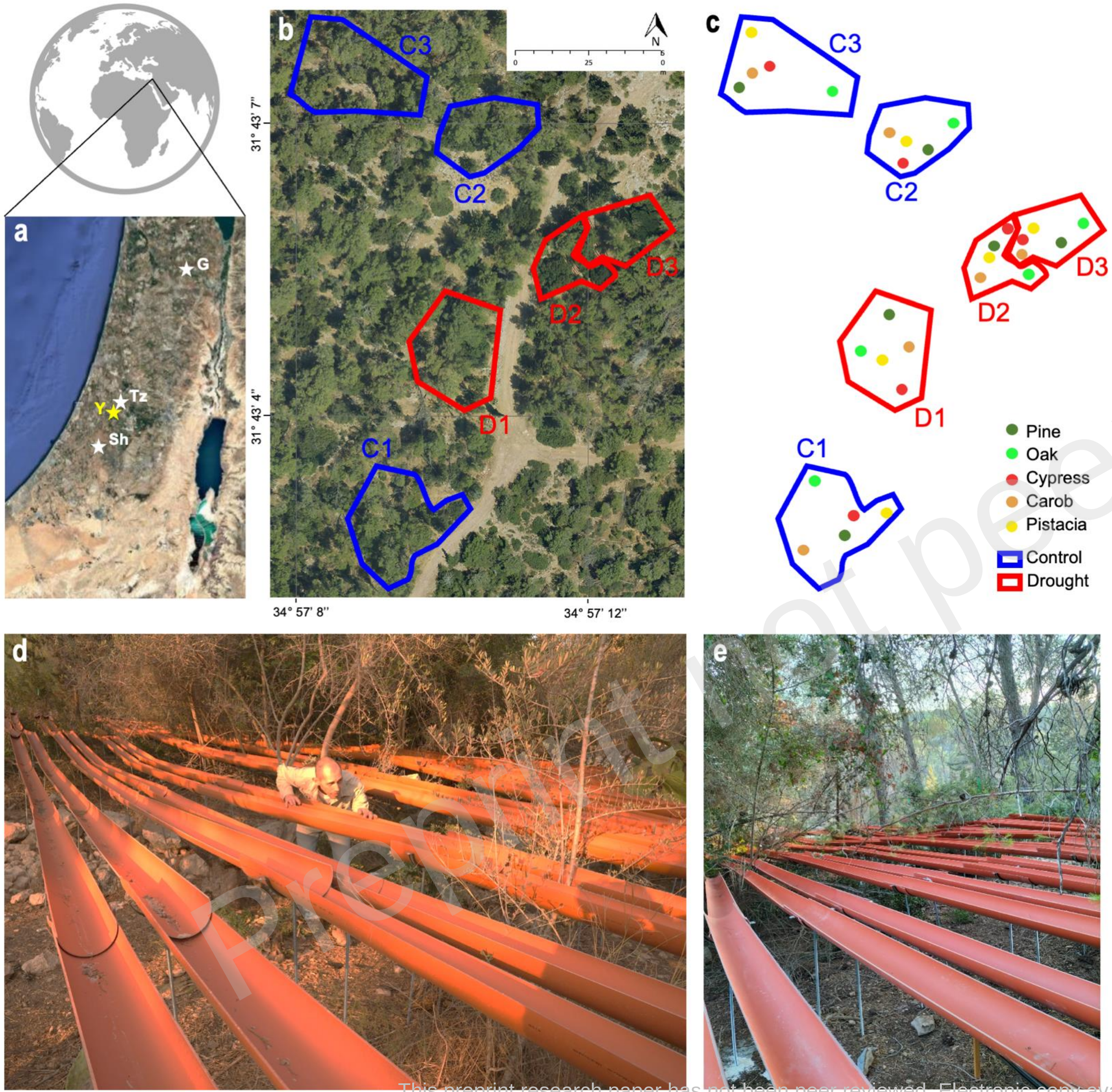


**Figure 1.** The study area showing **(a)** the experimental site of Yishi forst (Y; yellow star) and the three forest sites of Tzora (Tz), Shacharia (Sh), and Gilboa (G). **(b)** Aerial view of the 0.05-hectare plots at Yishi, with control plots in blue (C1-C3) and rainfall exclusion plots in red (D1-D3). **(c)** Same as (b) but with the tree species marked on the map. (**d–e**) The rainfall exclusion system in Yishi consisting of open-pipe gutters installed to divert approximately 50% of incident precipitation.

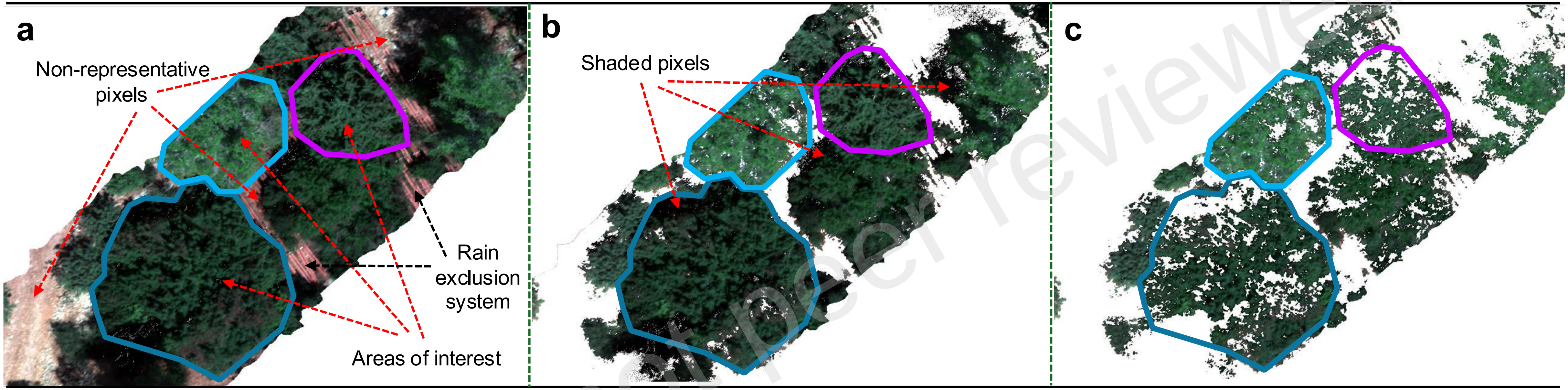


**Figure 2.** Hyperspectral image preprocessing workflow for isolating tree canopy pixels, showing **(a)** original image of experimental plots with outlined areas of interest (canopy), non-representative pixels, and visible components of the rainfall exclusion system (black arrows). At first, (b) non-vegetated pixels are removed using an NDVI threshold of <0.3. (c) Then, to remove the shaded canopy portions, the near-infrared reflectance threshold of 0.07-0.2 was used.

**Figure 3.** Workflow of the modeling framework, illustrating the use of inputs comprising 274 spectral bands from hyperspectral imagery and labeled drought/control trees, which were partitioned into training (70%) and test (30%) sets. The training data follows two parallel processing paths: **(1)** the hyperspectral pathway (left) where machine learning models are trained, followed by feature importance analysis and dimensionality reduction to retain bands representing 80% cumulative importance with 10 nm separation, resulting in refined hyperspectral models; and **(2)** the satellite simulation pathway (right) where synthetic satellite bands are created to train satellite-compatible models. Both refined hyperspectral and satellite models are evaluated using the same held-out test set to assess classification performance for drought stress detection.

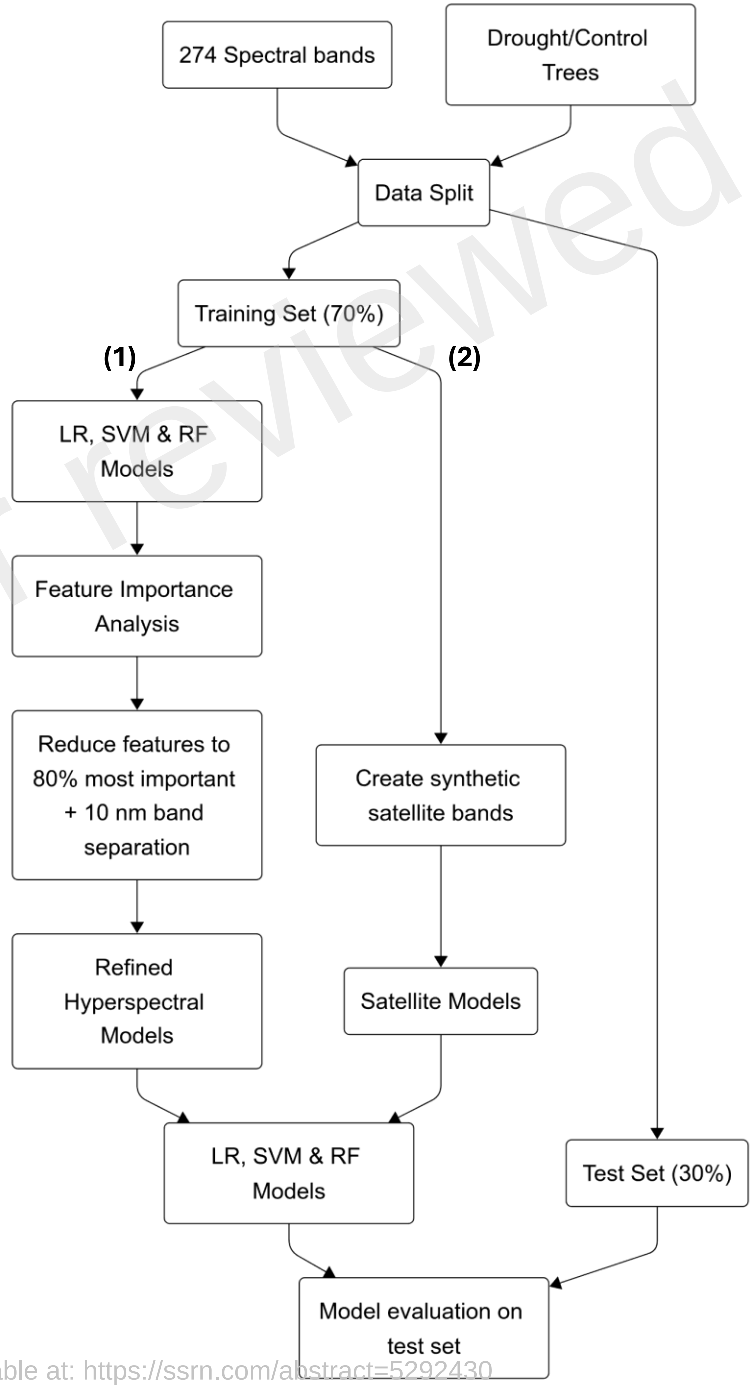

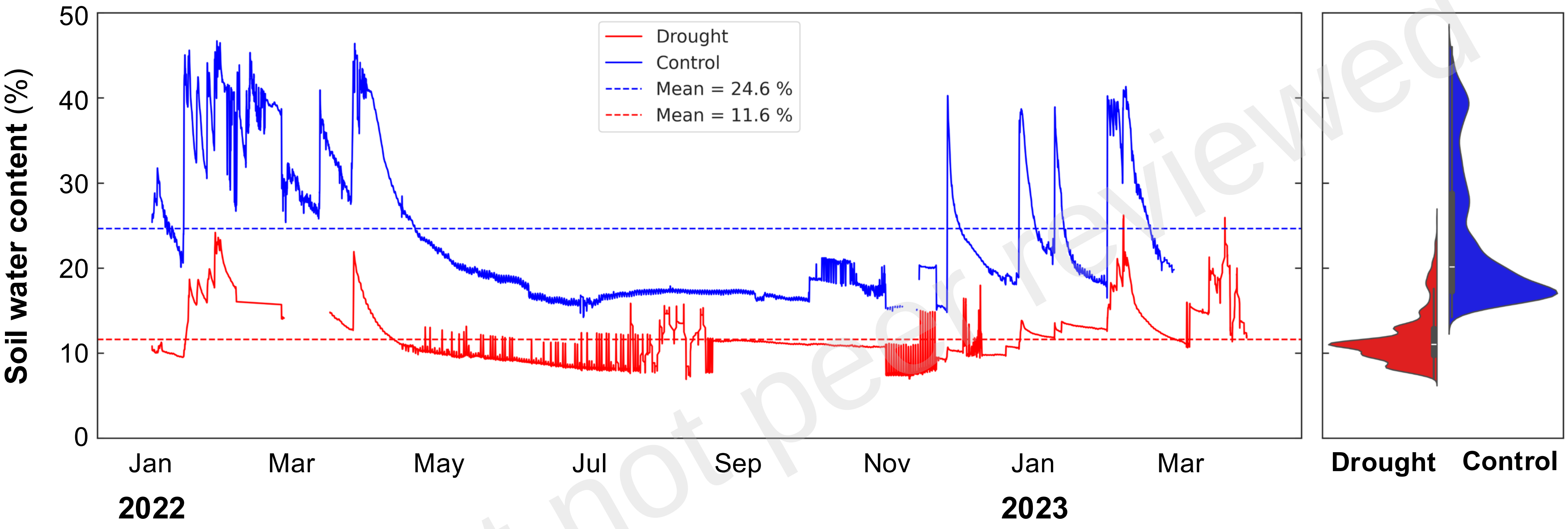


**Figure 4.** Soil water content (SWC; %) dynamics in control and rainfall exclusion plots over the experimental period. The blue line represents the averaged SWC in control plots, and the red one represents the SWC in rainfall exclusion plots from January 2022 to March 2023. Horizontal dashed lines indicate the mean values across the entire period. The violin plot on the right displays the full distribution of soil moisture measurements for each treatment. Data were smoothed using a Savitzky-Golay filter with a window length of 21 and a polynomial order of 3 to improve the visualization of temporal trends.

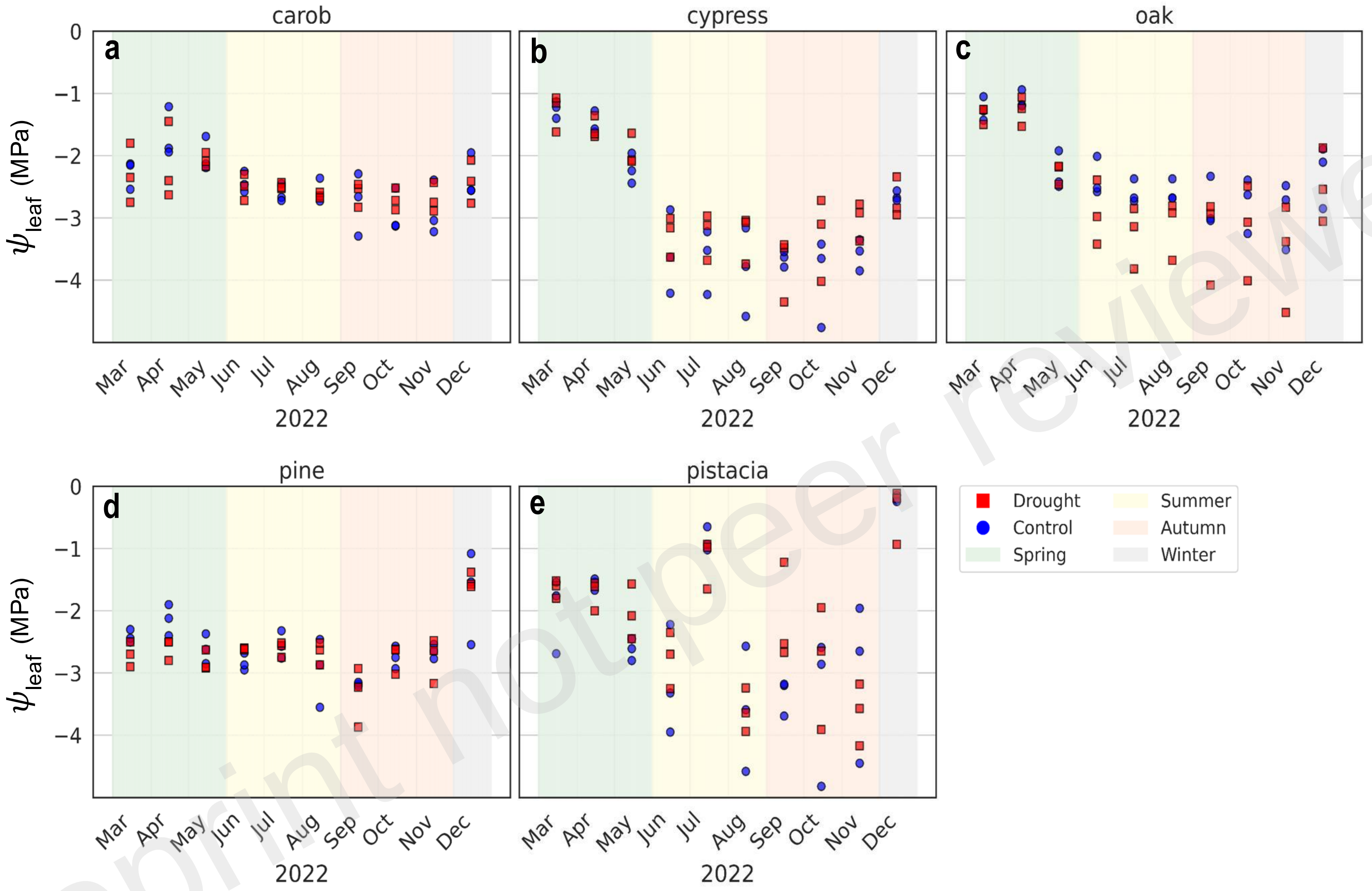


**Figure 5.** Leaf water potential ($\psi_{leaf}$) measurements across the five species under control and rainfall exclusion treatments. Scatter plots showing $\psi_{leaf}$ (MPa) for **(a)** carob, **(b)** cypress, **(c)** oak, **(d)** pine, and **(e)** pistacia from March to December 2022. Each point represents an individual tree measurement, with control trees denoted by blue circles and drought-treated trees by red squares. Background colors indicate seasons: spring (green, March-May), summer (yellow, June-August), autumn (light red, September-November), and winter (gray, December-February).

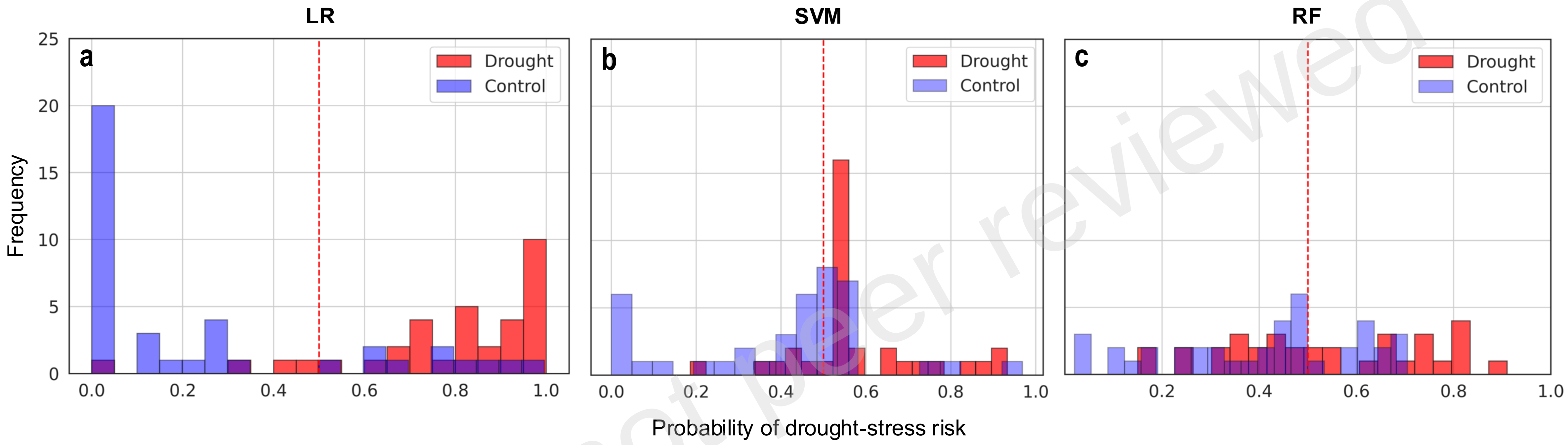


**Figure 6.** Histograms showing the frequency of predicted drought-stress risk probabilities for **(a)** Logistic Regression (LR), **(b)** Support Vector Machine (SVM), and **(c)** Random Forest (RF) models applied to the test dataset (N=74). Models were trained using a reduced hyperspectral feature set that contained only the top spectral bands, representing 80% of the cumulative importance. Blue bars represent control samples and red bars represent drought-treated samples. The vertical dashed red line at 0.5 indicates the classification threshold above which samples were classified as drought-stressed.

**Figure 7**. Application of SVM drought detection model to VENμS satellite imagery across three Mediterranean forest sites over multiple years. Each row represents a different forest: Tzora (top), Shacharia (middle), and Gilboa (bottom). Each column shows a different year (the year is indicated at the top right corner) with paired images: upper panels display the model's drought risk prediction (blue = low risk, red = high risk) and lower panels show corresponding RGB satellite imagery. White rectangular outlines (A and B) highlight areas of interest where the model predicted high drought stress risk (red pixels) before visible decline was visible. The color bar on the right indicates drought stress risk probability from 0 (low, blue) to 1 (high, red).

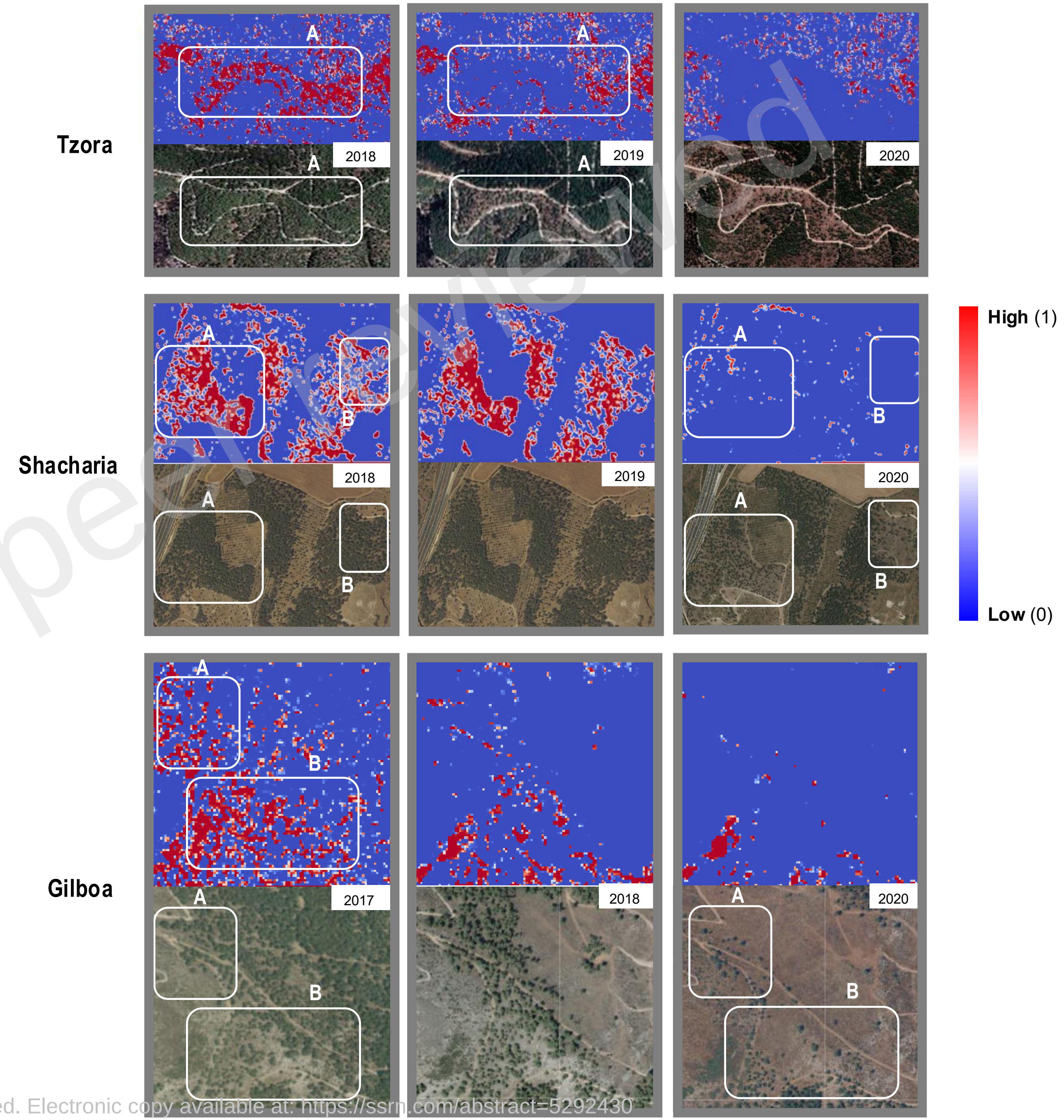

# Supplement

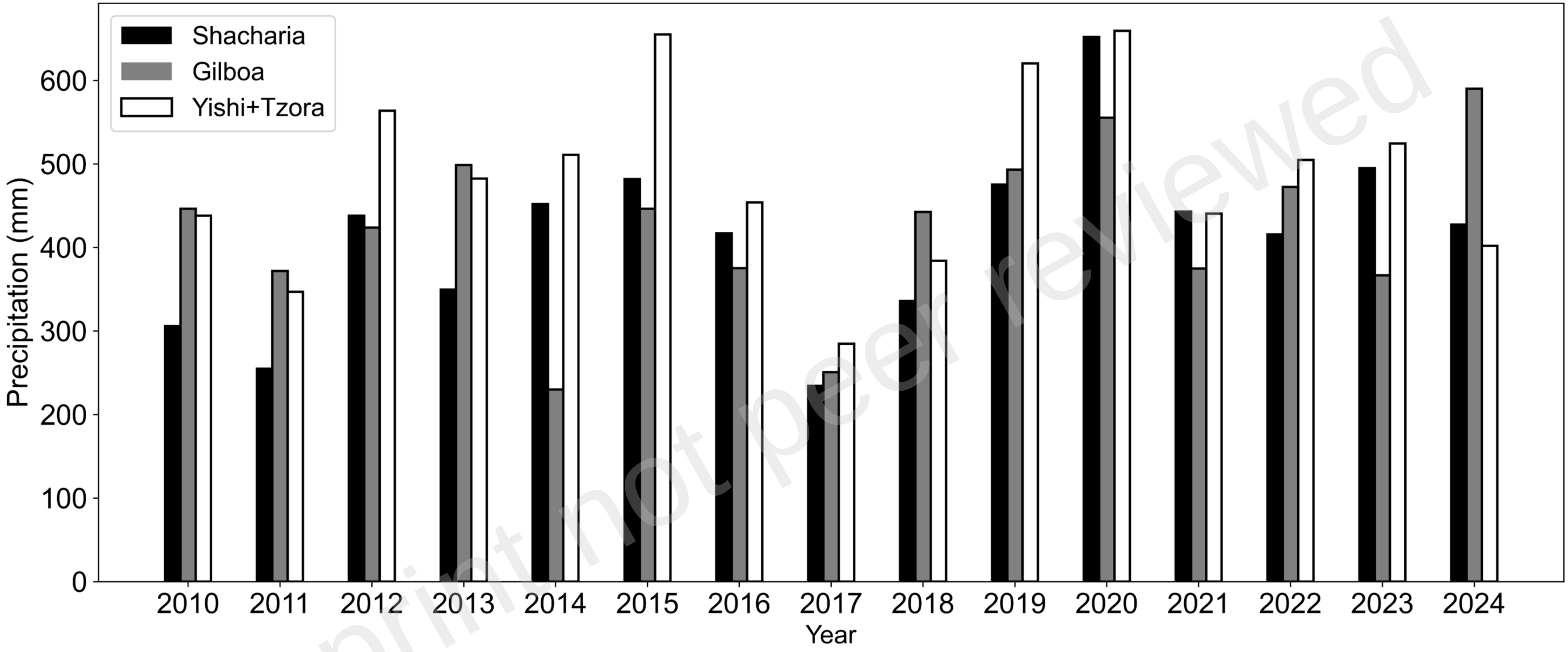


**Figure S1. Annual precipitation at the three study sites from 2010 to 2024.** Bar chart showing total annual precipitation (mm) recorded at meteorological stations near Shacharia (black), Gilboa (gray), and Yishi+Tzora (white) forests. Data were obtained from the Israel Meteorological Service stations located 4.8 km, 7.5 km, and 5.8 km from the respective forest sites. The year 2017 shows notably lower precipitation across all sites, representing a severe drought event that was used for model validation.

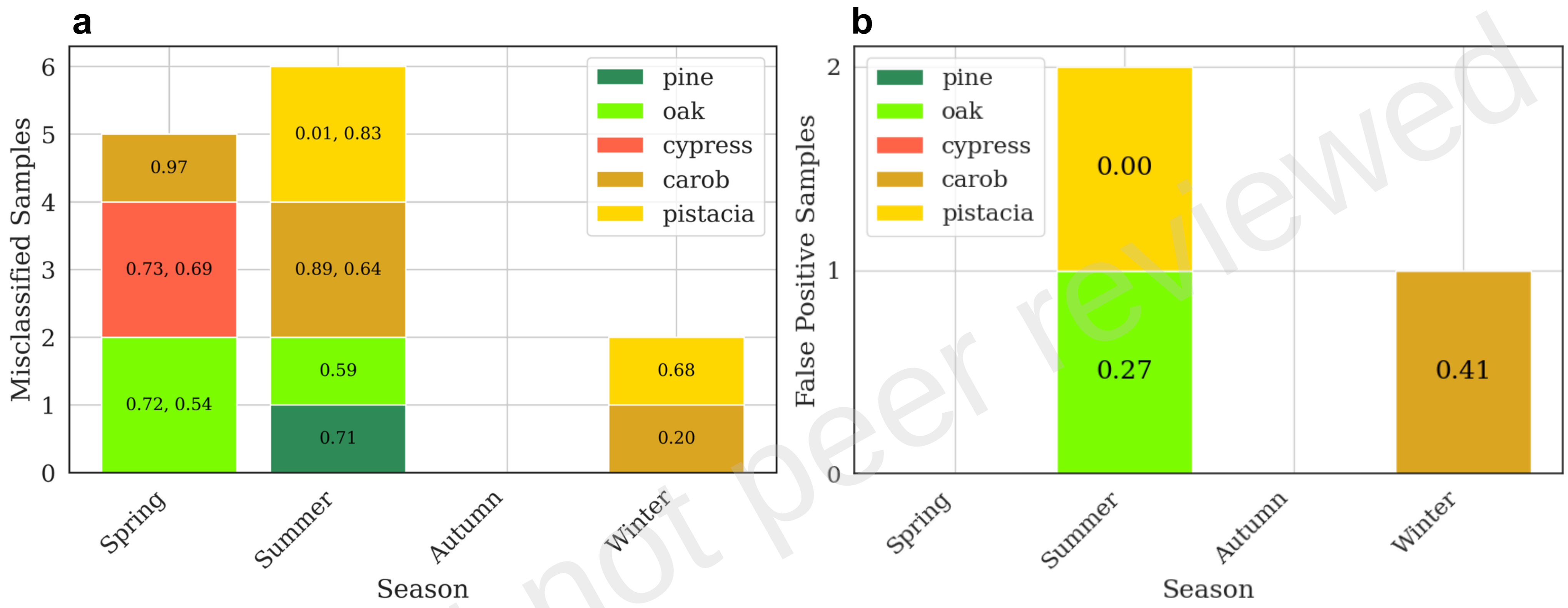


**Figure S2.** Seasonal distribution of misclassified samples from the Logistic Regression model with 80% feature importance. **(a)** Stacked bar chart showing all misclassified samples by season (spring, summer, autumn, winter) and tree species (pine, oak, cypress, carob, pistacia), with numbers indicating the model's drought probability score for each misclassified sample. (b) Stacked bar chart displaying only false positive samples (drought-stressed samples incorrectly classified as control) by season and species, with probability scores shown inside each bar segment. The number represents the score that the model assigned to each sample, where scores above 0.5 (50%) resulted in classification as drought-stressed.

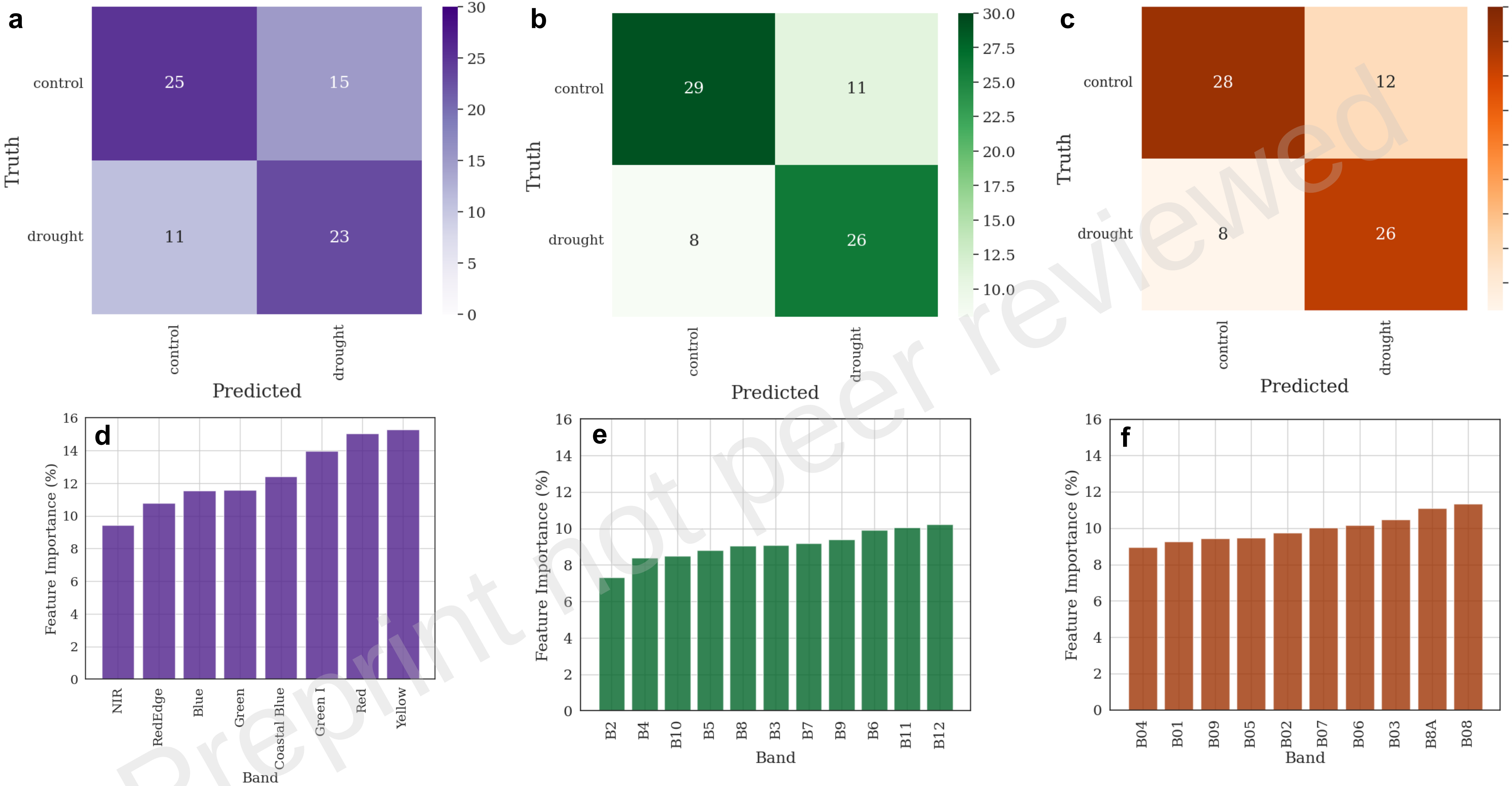


**Figure S3**. Confusion matrices and feature importance for SVM models trained on synthetic satellite spectral data. The top row shows confusion matrices for **(a)** Planet, **(b)** VENµS, and **(c)** Sentinel-2 satellite bands, displaying the number of samples correctly and incorrectly classified in each category (control vs. drought). Numbers in each cell represent the count of samples. Bottom row shows feature importance (%) for **(d)** Planet (purple), **(e)** VENµS (green), and **(f)** Sentinel-2 (orange) satellite bands.